

ENVIRONMENTALLY DRIVEN GLOBAL EVOLUTION OF GALAXIES

RENYUE CEN

Princeton University Observatory, Princeton, NJ 08544, USA; cen@astro.princeton.edu

Received 2011 April 30; accepted 2011 July 26; published 2011 October 24

ABSTRACT

Utilizing *high-resolution large-scale* galaxy formation simulations of the standard cold dark matter model, we examine global trends in the evolution of galaxies due to gravitational shock heating by collapse of large halos and large-scale structure. We find two major global trends. (1) The mean specific star formation rate (sSFR) at a given galaxy mass is a monotonically increasing function with increasing redshift. (2) The mean sSFR at a given redshift is a monotonically increasing function of decreasing galaxy mass that steepens with decreasing redshift. The general dimming trend with time merely reflects the general decline of gas inflow rate with increasing time. The *differential* evolution of galaxies of different masses with redshift is a result of gravitational shock heating of gas due to formation of large halos (groups and clusters) and large-scale structure that moves a progressively larger fraction of galaxies and their satellites into environments where gas has too high an entropy to cool to continue feeding resident galaxies. Overdense regions where larger halos are preferentially located begin to be heated earlier and have higher temperatures than lower density regions at any given time, causing sSFR of larger galaxies to fall below the general dimming trend at higher redshift than less massive galaxies and galaxies with high sSFR to gradually shift to lower density environments at lower redshift. We find that several noted cosmic downsizing phenomena are different manifestations of these general trends. We also find that the great migration of galaxies from blue cloud to red sequence as well as color–density relation, among others, may arise naturally in this picture.

Key words: cosmology: theory – galaxies: clusters: intracluster medium – galaxies: evolution – galaxies: groups: general – hydrodynamics – methods: numerical

Online-only material: color figures

1. INTRODUCTION

The intriguing phenomenon of the so-called cosmic downsizing (e.g., Cowie et al. 1996) has had practitioners of the cold dark matter cosmogony perplexed. Innovative astrophysical ideas have been proposed to introduce scales in the growth of galaxies within the context of hierarchical formation of dark matter halos in the standard cosmological constant-dominated cold dark matter model (LCDM; Komatsu et al. 2011). Successful models have been constructed, for example, semi-analytically by incorporating possible active galactic nucleus (AGN) feedback (e.g., Croton et al. 2006; Bower et al. 2006).

In this work we investigate the nature of cosmic downsizing in the LCDM model by performing and analyzing *high-resolution large-scale* hydrodynamic galaxy formation simulations, including feedback from star formation (SF) and proper treatment of gravitational heating due to collapse of large-scale structure. Our simulations reproduce well observations that galaxies of higher star formation rates (SFRs) contribute progressively more to the overall SFR density toward higher redshift (e.g., Cowie et al. 1996). We find that this cosmic downsizing phenomenon is part of a fundamental and universal trend that the specific star formation rate (sSFR), *on average*, is a monotonic function of galaxy halo (or stellar) mass with lower-mass galaxies having higher sSFR. As a result, *on average*, the stellar mass doubling time is a monotonically decreasing function with decreasing stellar mass at any redshift and for more massive galaxies that upcrosses the Hubble time earlier than less massive galaxies. The sSFR of galaxies of all masses, *on average*, display a monotonic and mass-dependent rate of increase with redshift. In this sense, we see primarily a trend of “differential galaxy dimming” from high redshift to $z = 0$. Although the sSFR trend continues to the highest redshift we have examined, the SFR

density that is a convolution of these trends and halo abundance evolution in the cold dark matter model displays a maximum at $z = 1.5$ – 2 . Related, within the simulation volume and density fluctuations that we probe, we also see an “upsizing” trend at $z \geq 2$ in that the maximum SFR of galaxies decreases toward still higher redshift, probably reflecting the tenet of the standard cold dark matter model of hierarchical buildup of dark matter halos where the abundance of very large halos starts to drop off exponentially.

We examine the underlying physical cause for these distinct trends. We find that at high redshift ($z \geq 2$) SF is largely gas demand limited, where there is sufficient supply of cold gas for galaxies to double its stellar mass within a Hubble time and SF is mostly regulated by its own efficiency, due to feedback effects from SF. At $z \leq 2$ SF gradually moves to the regime of being supply limited, dependent on environments, as the supply rate of cold gas decreases, due to a combination of primarily two factors. First, the overall decrease of density [$\propto (1+z)^3$] (and to a minor degree of characteristic velocity at a fixed halo mass) causes the gas inflow rate to decline with decreasing redshift. Second, the overall heating of cosmic gas due to formation of large halos (such as groups and clusters) and large-scale structures causes a progressively larger fraction of halos to inhabit regions where gas has too high an entropy to cool to continue feeding the residing galaxies. The combined effect is *differential* in that overdense regions are heated earlier and to higher temperatures than lower density regions at any given time. Because larger halos tend to reside, in both a relative and an absolute sense, in more overdense regions than smaller halos, the net differential effects are that larger galaxies fall below the general dimming trend at higher redshift than less massive galaxies, the sSFR as a function of galaxy mass steepens with time and galaxies with the high sSFR gradually shift to

lower density environments. We do include supernova feedback in the simulations and find that galactic winds are strong for starburst galaxies, strongest at $z \geq 2$ when SF activities are most vigorous, and are stronger in less massive galaxies than in large galaxies. But it appears that the stellar feedback processes do not drive any noticeable trend of the sort presented here, although they are important in self-regulating SF at high redshift when gas supply rate is high.

The findings summarized above need to be placed in the context of the current theory of galaxy formation with respect to gas accretion. Galaxies need to acquire gas continuously to sustain observed SF (e.g., Bauermeister et al. 2010). The current standard theory of gas accretion hinges on the cold and hot two-mode accretion model, based on the pioneering work of Kereš et al. (2005) and Dekel & Birnboim (2006). The crux of the theory is that halo mass is the sole determinant of gas accretion: large halos ($M_h \geq$ a few $10^{11} M_\odot$) primarily accrete hot gas while small halos primarily accrete cold gas. The division halo mass between the two modes of accretion is roughly redshift independent. Subsequently, additions have been made by the original authors to the theory to allow some large halos (above the division halo mass) to accrete cold gas at high redshift to accommodate SF in them that is observed. This widely accepted paradigm is, however, still fundamentally incomplete. Simply put, while halo mass is a basic independent variable, the process of gas accretion is a multivariant function. It also depends, critically, on the halo environment on intermediate scales (~ 2 Mpc), and this dependence can explain the observed phenomenon of cosmic downsizing.

We also find that the cold gas starvation due to gravitational heating provides a natural mechanism to explain the observed migration of galaxies to the red sequence from the blue cloud as well as many other phenomena, such as the observed color–density relation, the trend of galaxies becoming bluer in lower density environments, and others.

The outline of this paper is as follows. In Section 2 we detail our simulations, method of making galaxy catalogs, and analysis methods. Results are presented in Section 3. In Section 3.1 we compare some basic galaxy observables to observations. In Section 3.2 we present detailed results of galaxy evolution and compare them to observations. We then examine and understand physical processes that are primarily responsible for the results obtained in Section 3.3, followed by predictions of the model in Section 3.4. Conclusions are given in Section 4.

2. SIMULATIONS

2.1. Hydrocode and Simulation Parameters

We perform cosmological simulations with the adaptive mesh refinement (AMR) Eulerian hydrocode Enzo (Bryan 1999; Bryan & Norman 2000; O’Shea et al. 2004; Joung et al. 2009). First, we ran a low-resolution simulation with a periodic box of $120 h^{-1}$ Mpc on a side. We identified two regions separately, one centered on a cluster of mass of $\sim 2 \times 10^{14} M_\odot$ and the other centered on a void region at $z = 0$. We then resimulate each of the two regions separately with high resolution, but embedded in the outer $120 h^{-1}$ Mpc box to properly take into account large-scale tidal field and appropriate boundary conditions at the surface of the refined region. We name the simulation centered on the cluster “C” run and the one centered on the void “V” run. The refined region for “C” run has a size of $21 \times 24 \times 20 h^{-3}$ Mpc³ and that for “V” run is $31 \times 31 \times 35 h^{-3}$ Mpc³. At their respective

volumes, they represent 1.8σ and -1.0σ fluctuations. The initial condition in the refined region has a mean interparticle separation of $117 h^{-1}$ kpc comoving, dark matter particle mass of $1.07 \times 10^8 h^{-1} M_\odot$. The refined region is surrounded by two layers (each of $\sim 1 h^{-1}$ Mpc) of buffer zones with particle masses successively larger by a factor of eight for each layer, which then connects with the outer root grid that has a dark matter particle mass 8^3 times that in the refined region. Because we still cannot run a very large volume simulation with adequate resolution and physics, we choose these two runs to represent two opposite environments that possibly bracket the average. As we have shown in Cen (2010), these two runs indeed bracket all compared observables of damped Lyman alpha systems (DLAs) and tests show good numerical convergence.

We choose the mesh refinement criterion such that the resolution is always better than $460 h^{-1}$ pc physical, corresponding to a maximum mesh refinement level of 11 at $z = 0$. The simulations include a metagalactic UV background (Haardt & Madau 1996) and a model for shielding of UV radiation by neutral hydrogen (Cen et al. 2005). They also include metallicity-dependent radiative cooling (Cen et al. 1995). Star particles are created in cells that satisfy a set of criteria for SF proposed by Cen & Ostriker (1992). Each star particle is tagged with its initial mass, creation time, and metallicity; star particles typically have masses of $\sim 10^6 M_\odot$.

Supernova feedback from SF is modeled following Cen et al. (2005). Feedback energy and ejected metal-enriched mass are distributed into 27 local gas cells centered at the star particle in question, weighted by the specific volume of each cell, which is to mimic the physical process of supernova blast wave propagation that tends to channel energy, momentum, and mass into the least dense regions (with the least resistance and cooling). We allow the entire feedback processes to be hydrodynamically coupled to surroundings and subject to relevant physical processes, such as cooling and heating. The total amount of explosion kinetic energy from Type II supernovae for an amount of star formed M_* with a Chabrier initial mass function (IMF) is $e_{\text{SN}} M_* c^2$ (where c is the speed of light) with $e_{\text{GSW}} = 6.6 \times 10^{-6}$. Taking into account the contribution of prompt Type I supernovae, we use $e_{\text{SN}} = 1 \times 10^{-5}$ in our simulations. Observations of local starburst galaxies indicate that nearly all of the SF produced kinetic energy is used to power GSW (galactic superwinds; e.g., Heckman 2001). Supernova feedback is important primarily for regulating SF and for transporting energy and metals into the intergalactic medium. The extremely inhomogeneous metal enrichment process demands that both metals and energy (and momentum) are correctly modeled so that they are transported in a physically sound (albeit still approximate at the current resolution) way. The kinematic properties traced by unsaturated metal lines in DLAs are extremely tough tests of the model, which is shown to agree well with observations (Cen 2010). As we will show below, the properties of galaxies produced in the simulations resemble well-observed galaxies, within the limitations of finite resolution. In order not to mingle too many different effects, we do not include any feedback effect from an AGN, which is often invoked to suppress SF by cooling from hot atmosphere in large galaxies. We will see later that this omission may have caused larger galaxies to be somewhat overluminous.

We use the following cosmological parameters that are consistent with the *Wilkinson Microwave Anisotropy Probe* seven-year-results-normalized (Komatsu et al. 2011) LCDM

model: $\Omega_M = 0.28$, $\Omega_b = 0.046$, $\Omega_\Lambda = 0.72$, $\sigma_8 = 0.82$, $H_0 = 100 h \text{ km s}^{-1} \text{ Mpc}^{-1} = 70 \text{ km s}^{-1} \text{ Mpc}^{-1}$, and $n = 0.96$.

2.2. Simulated Galaxy Catalogs

We identify galaxies in our high-resolution simulations using the HOP algorithm (Eisenstein & Hu 1999), operated on the stellar particles, which is tested to be robust and insensitive to specific choices of concerned parameters within reasonable ranges. Satellites within a galaxy are clearly identified separately. The luminosity of each stellar particle at each of the Sloan Digital Sky Survey (SDSS) five bands is computed using the GISSEL stellar synthesis code (Bruzual & Charlot 2003) assuming a Salpeter IMF, by supplying the formation time, metallicity, and stellar mass. Collecting luminosity and other quantities of member stellar particles, gas cells, and dark matter particles yields the following physical parameters for each galaxy: position, velocity, total mass, stellar mass, gas mass, mean formation time, mean stellar metallicity, mean gas metallicity, SFR, luminosities in five SDSS bands (and various colors), and others.

For each galaxy we also compute its intermediate-scale environmental overdensity, defined to be the dark matter density, smoothed by a Gaussian function of radius $2 h^{-1} \text{ Mpc}$ comoving, divided by the global mean dark matter density. We choose this smoothing scale because it encloses a mass of $1.3 \times 10^{13} h^{-1} M_\odot$, whose gas at virial radius shock heated to the virial temperature approximately corresponds to the critical entropy S_{crit} that is a weak function of redshift. The relevance of S_{crit} will be explained in Section 3.2. In addition, we compute the mean gas entropy of each galaxy at its virial radius, defined as $\langle S \rangle = \sum T n^{1/3} dV / \sum n dV$, where the two sums are over cells whose galactocentric radius falls in the radial range $(0.9-1.1)r_v$ (r_v is the virial radius), and T , n , and dV are gas temperature, number density, and the volume of each cell, respectively. We also compute various fluxes across the virial radius for each galaxy, including the total gas mass flux and cold mass flux. The mass flux is computed as $\langle F_m \rangle = \sum 4\pi r^2 v_r \rho / \sum \text{cells}$, where the two sums are over all cells in the radial range $(0.9-1.1)r_v$, r is the galactocentric radius, v_r is radial velocity (positive for outflow and negative for inflow), and ρ is gas mass density. The thickness of this radial shell ranges $((0.9-1.1)r_v)$ from $10 \text{ kpc } h^{-1}$ to $100 \text{ kpc } h^{-1}$ for galaxies of interest here, which is much larger than our spatial resolution. So we simply sum up all cells whose centers are within this radial range.

3. RESULTS

3.1. Validating Simulated Galaxies

This is a first-in-its-class kind of galaxy formation simulation that includes sophisticated physical treatment, sufficient resolution, and a large enough sample covering the entire redshift range to statistically address relevant questions. Simulations by various workers in the field have significantly advanced in recent years, but there has been a gap between a large sample of galaxies and sufficient numerical resolution. There are two camps because of this gap. In the first camp, efforts are devoted to idealized and isolated boundary-condition individual or galaxy merger simulations (e.g., Hopkins et al. 2006; Mayer et al. 2007) with very high resolution. In the second camp, simulations are “cosmological” but primarily focus on a few individual galaxies with high resolution of $\sim 50-100 \text{ pc}$ (e.g., Governato et al. 2009; Gnedin et al. 2009; Ceverino et al. 2010) and frequently do not reach $z = 0$. Truly cosmological simulations with a large sample size need to strike a compromise between galaxy sample

size, particle mass, and spatial resolution. The state-of-the-art simulations of Davé et al. (2010) employ dark matter particles that are about a factor five more massive, spatial resolution about a factor of two lower than in this study, and do not reach $z = 0$.

Our simulations are ground breaking primarily in two areas. First, they have a large sample (thousands) of galaxies and run all the way to $z = 0$, while maintaining an excellent sub-kiloparsec resolution that is adequate for many cosmological applications, including this study. Second, we follow SF feedback in a physically sound fashion that does not resort to “tricks,” such as hydrodynamic decoupling between supernova ejecta and ambient gas or suppression of gas cooling following supernova explosions that are frequently used in some simulations. The first of these is achieved by improving our numerical algorithms, while the second is crucial to ensure that the amount of stellar feedback is close to what it should be.

This second issue is most difficult to ascertain. One objective but indirect way to verify this is to test the consequences of the feedback scheme. In Cen (2010) we presented a detailed examination of the DLAs and found that the simulations, for the first time, are able to match all observed properties of DLAs, including abundance, size, metallicity, and kinematics. The broad agreement between simulations and observations suggests that our treatment of feedback processes (including metal enrichment and transport) is realistic; other simulations that do not include this detailed treatment (such as metal transport) do not provide as good agreement with observations as ours especially with respect to kinematics (which depends quite sensitively on metallicity distribution). While the results in this paper do not sensitively directly depend on gas metallicity, the fact that the simulations pass this stringent test indicates that the amount of energy and dynamics that drive metal transport by stellar feedback is realistic. Nevertheless, as with any simulation, there are limitations. As such, it is prudent to examine the basic properties of galaxies themselves in the simulations to gauge how realistically we can reproduce observations.

Figure 1 shows the SFR density history from $z = 0$ to $z = 6$. We see that for the entire redshift range the SF histories from C and V runs bracket the observations, suggesting that the SFR histories in the simulations are consistent with the extant observations. It is probably true that the global average lies between these two runs. However, the weightings of two runs for averaging are likely complicated because different properties of galaxies of different masses depend on large-scale environments in a non-trivial fashion. For brevity, we use the constraints from the observed SFRD history to obtain our “best” weightings for C and V runs; we find a weighting for the C run equal to $(1+z)/(7+z)$ (with one minus that for the V run) to fit the redshift range of interest here, with the obtained average SFR density shown as the blue curve in Figure 1. In some of the subsequent figures, we use the same weightings to average over some quantities of the two runs, when such an exercise is preferential.

Figure 2 shows the SDSS rest-frame $g-r$ color distribution of galaxies at $z = 0, 1.0, 1.6$. The averaged color distribution at each redshift is obtained by the same weighting scheme normalized to the SFR density evolution in Figure 1. We see that the simulations can reproduce the observed bimodality well at $z = 0$ (Blanton et al. 2003a); varying the weightings of the two runs in averaging within any reasonable range does not alter the bimodal nature of the distribution. There is a hint that our simulated galaxies may be slightly too blue

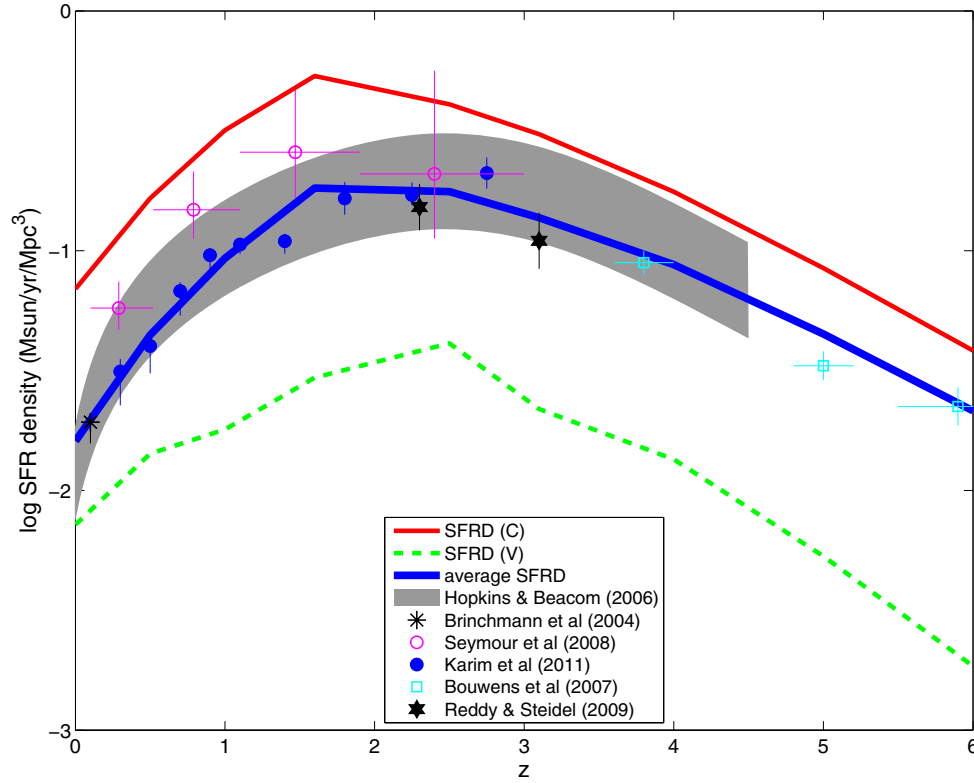


Figure 1. Evolution SFR density from C (red solid curve) and V (green dashed curve) runs. Also shown as the gray shaded region are the observations compiled by Hopkins & Beacom (2006), as blue points and magenta circles two more recent observations using radio techniques from Karim et al. (2011; 2σ error bars) and Seymour et al. (2008; 1σ error bars), as a black asterisk the local SDSS data from Brinchmann et al. (2004; 1σ error bars), as two black hexagons from Reddy & Steidel (2009; 1σ error bars), and as open blue squares from Bouwens et al. (2007; 1σ error bars). The blue curve is an average of the two runs. Simulation results and observational data are all based on the standard Salpeter IMF.

(A color version of this figure is available in the online journal.)

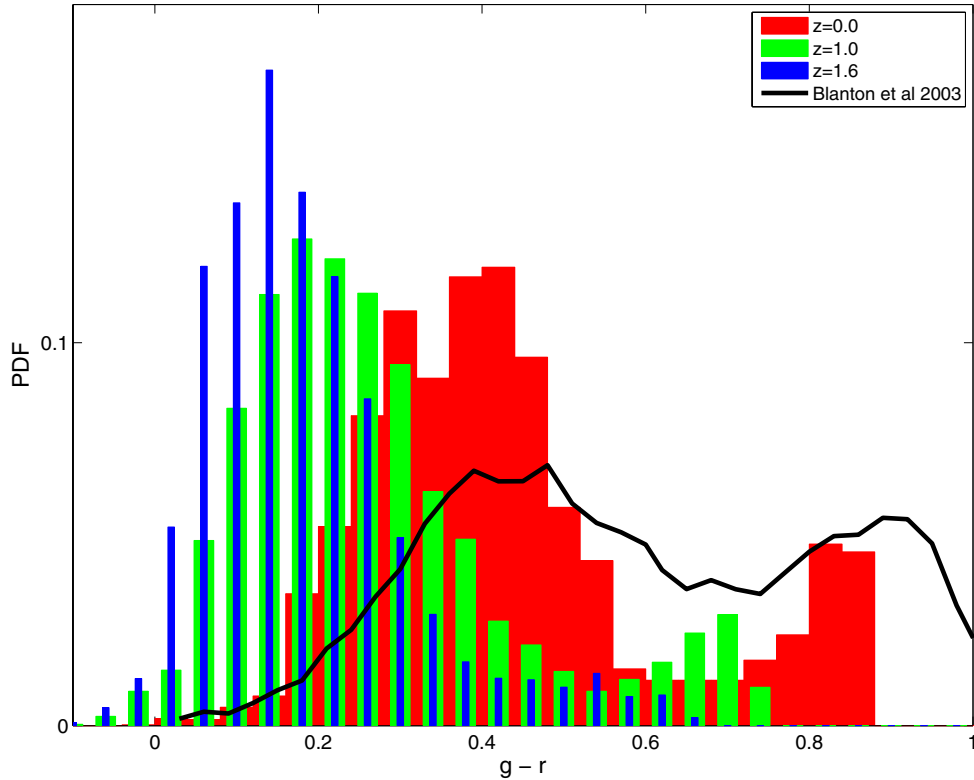


Figure 2. SDSS rest-frame $g - r$ color distributions of simulated galaxies (number weighted) with stellar mass greater than $10^9 M_\odot$ at $z = 0, 1, 1.6$ (red, green, and blue, respectively). Also shown as the black curve is the corresponding SDSS observations at $z = 0.1$ from Blanton et al. (2003a).

(A color version of this figure is available in the online journal.)

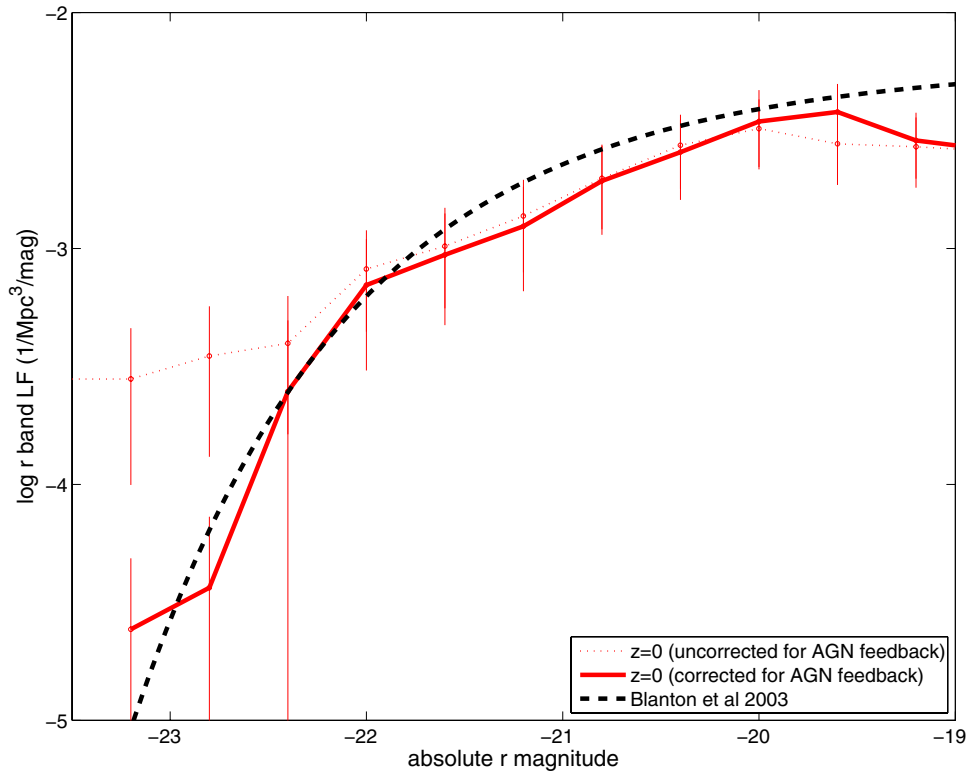


Figure 3. SDSS r -band galaxy luminosity function at $z = 0$. The thin dotted curve is directly from averaging over C and V runs, whereas the thick solid curve is obtained after correcting for AGN feedback. Also shown as the thick dashed curve is the Schechter fit to the SDSS data (Blanton et al. 2003b).

(A color version of this figure is available in the online journal.)

(by ~ 0.05 mag), which may be in part due to the omission of Type Ia supernova (SN) feedback on a longer timescale (~ 1 Gyr) in the present simulations (we include feedback from supernovae (SNe) II and prompt SNe Ia). Our future simulations including SNe Ia should verify this. Additionally, the overcooling problem in massive galaxies also contributes to enhancing the blue peak. There is evidence that the color bimodality persists at least to $z \sim 1$ with the relative strength of the red peak diminishing with increasing redshift consistent with observations (e.g., Weiner et al. 2005; Franzetti et al. 2007; Cirasuolo et al. 2007).

Figure 3 shows the SDSS g -band galaxy luminosity function at $z = 0$. Within the uncertainties the simulations agree reasonably well with observations, except at the high luminosity end where simulations overproduce luminous galaxies. This is a well-known problem in simulations that do not include some strong feedback in large galaxies. AGN feedback has been invoked to suppress SF due to cooling off of hot gas in large galaxies (e.g., Croton et al. 2006; Bower et al. 2006). If we apply a similar AGN feedback prescription as in Croton et al. (2006) by suppressing SF post-simulation by a factor of $f \equiv 1/(1 + (M_h/1.0 \times 10^{13} M_\odot)^{2/3})$, where we use $M_h = M_{\text{star}}/0.4$ for satellite galaxies whose halos can no longer be unambiguously delineated (while stellar identities remain largely intact), we obtain the result shown as the thick solid curve in Figure 3 that is in good agreement with observations. There is an indication that at $M_g > -19$, we underproduce small galaxies, which is probably a result of resolution effect. For the results that we present subsequently, these “defects” do not materially alter any conclusions that we draw, because we are mostly interested in the evolution of galaxies segregated in mass and in environments, which does not depend strongly on precise

abundances of galaxies. McCarthy et al. (2011) demonstrate the relatively mild effect of AGN feedback on gas entropy in the vicinity of virial radius.

Figure 4 shows the rest-frame UV (at 1700 \AA) luminosity functions at several redshifts, along with UV and IR (ultraluminous infrared galaxy and luminous infrared galaxy) observational data, to check if the reasonable agreement between simulations and observations found at lower redshift (Figures 2 and 3) extend to higher redshifts. We convert SFR of each simulated galaxy to $M_{\text{AB}}(1700 \text{ \AA})$ using the standard conversion formula, $\text{SFR} = 6.1 \times 10^{-[8+0.4M_{\text{AB}}(1700 \text{ \AA})]} M_\odot \text{ yr}^{-1}$ (Kennicutt 1998) in combination with the AB magnitude system (Oke 1974). We see that the simulations agree well with the UV observations for $M_{\text{AB}}(1700 \text{ \AA}) > -22$, within the uncertainties. A significant portion of the disagreement between simulations and UV data at $M_{\text{AB}}(1700 \text{ \AA}) < -22$ is removed when the abundance of ultra-luminous infrared galaxies (ULIRGs) is taken into account, and the simulations become approximately in agreement with observations within the errors at $M_{\text{AB}}(1700 \text{ \AA}) < -22$. The faint end slope of the UV luminosity functions appear to be steeper than $\alpha = -1.5$ and about $\alpha = -1.8$ to -1.7 , consistent with observations (e.g., Yan & Windhorst 2004; Bouwens et al. 2007; Reddy & Steidel 2009).

In summary, our simulations produce properties of galaxies in good agreement with a variety of observations that allow us now to examine their global evolutionary trends.

3.2. Global Trends of Galaxy Formation and Evolution

Figure 5 shows the cumulative light density distribution in the rest-frame SDSS z band as a function of absolute z magnitude

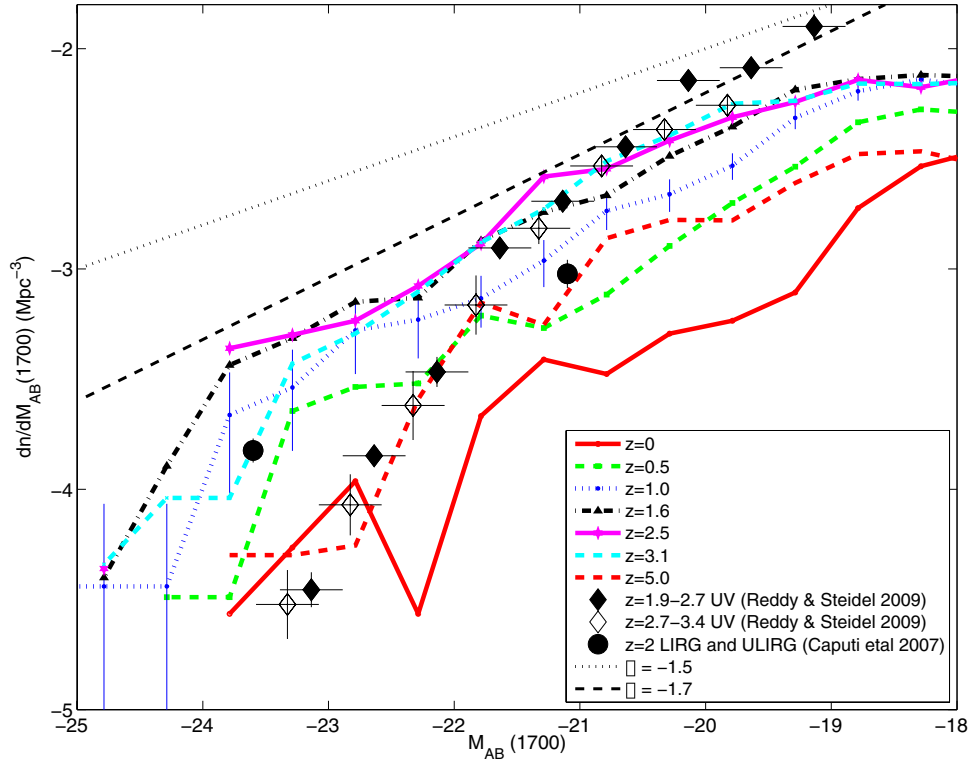


Figure 4. Rest-frame UV (at 1700\AA) luminosity functions at $z = 0, 0.5, 1.0, 1.6, 2.5, 3.1, 5$ with 1σ Poisson error bars indicated on the $z = 1$ curve. The UV observational data are from Reddy & Steidel (2009): solid diamonds at $z = 1.9\text{--}2.7$ and open diamonds at $z = 2.7\text{--}3.4$. Also shown as two solid dots are observed LIRG and ULIRG data from Caputi et al. (2007). The ULIRG and LIRG data points are shown, if they were not reprocessed through dust, to account for the fact that we do not process stellar light through dust grains. The dotted and dashed straight lines indicate the faint end slope of the luminosity function at $\alpha = -1.5$ and -1.7 , respectively.

(A color version of this figure is available in the online journal.)

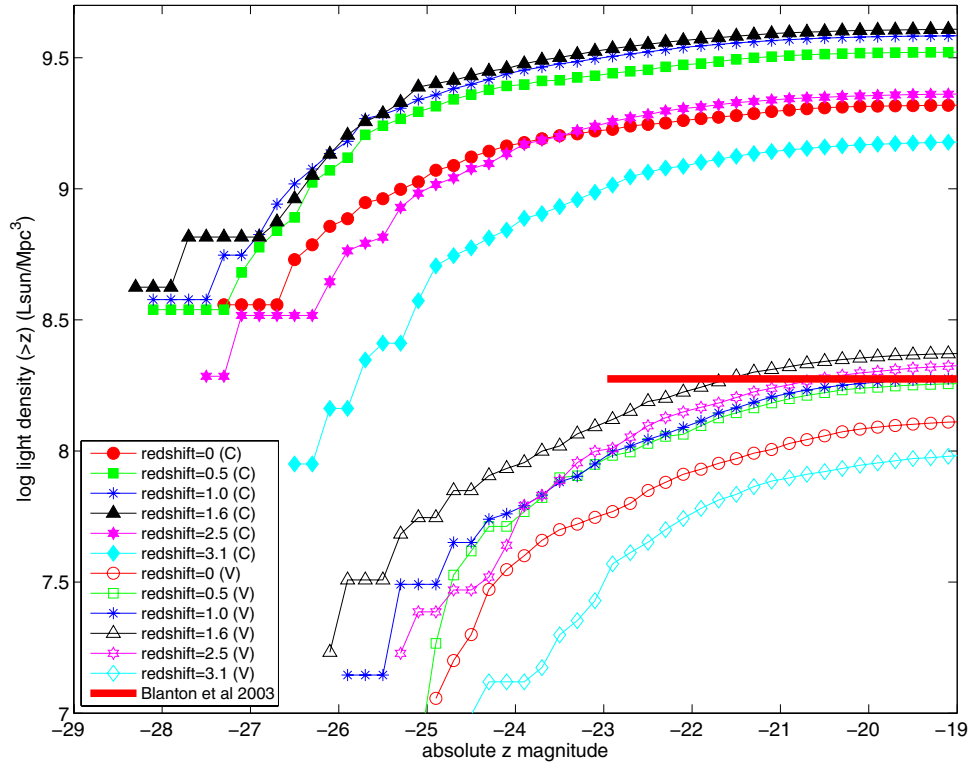


Figure 5. Cumulative light density distribution in rest-frame SDSS z band as a function of absolute z magnitude at redshifts $z = (0, 0.5, 1.0, 1.6, 2.5, 3.1)$ for both C and V runs. Also shown as the thick red horizontal solid line attached to the right y-axis is the value from SDSS data at $z \sim 0.1$ (Blanton et al. 2003b). Similar redshift trends are seen in other SDSS broadbands.

(A color version of this figure is available in the online journal.)

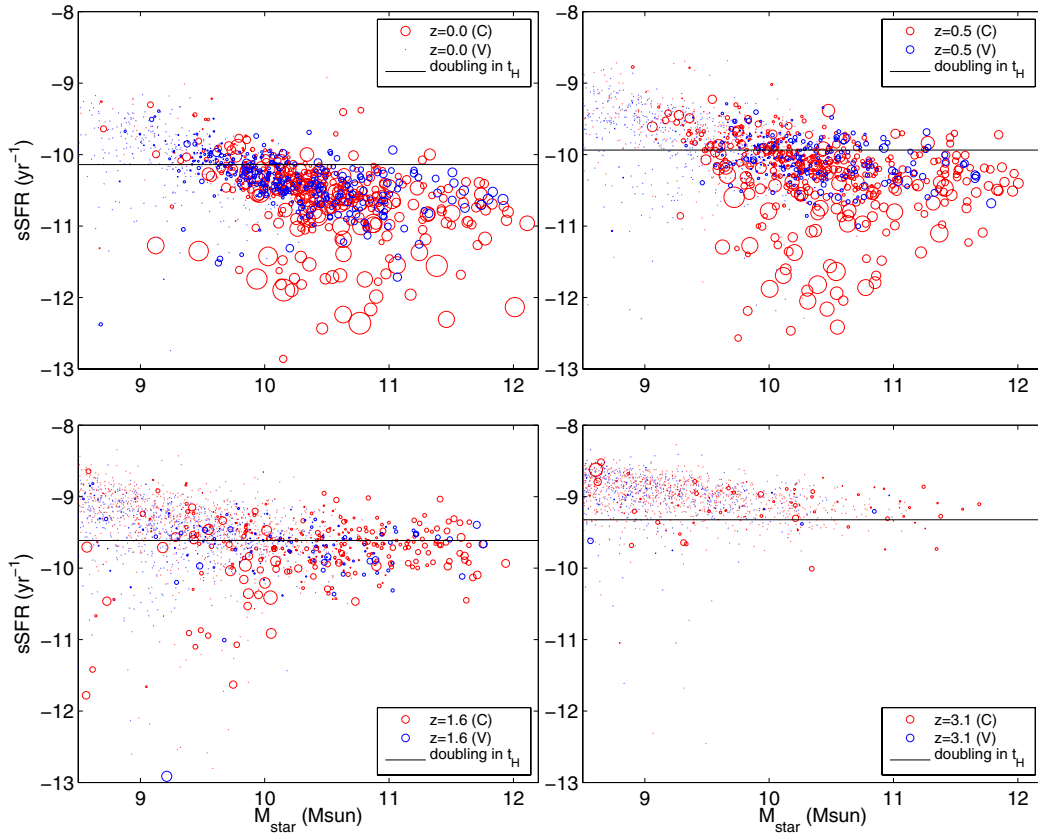


Figure 6. Scatter plot of sSFR vs. galaxy stellar mass at $z = 0$ (top left), $z = 0.5$ (top right), $z = 1.6$ (bottom left), and $z = 3.1$ (bottom right) for both C (red) and V (blue) runs. Each circle is a galaxy from C (red) and V (blue) runs with its size proportional to the logarithm of the gas entropy at its virial radius. The horizontal line in each panel indicates the sSFR value at which a galaxy would double its stellar mass in a Hubble time.

(A color version of this figure is available in the online journal.)

from redshift $z = 0$ to $z = 3.1$. The fact that the redshift $z = 0$ values of the two runs bracket the SDSS data at redshift $z \sim 0.1$ is self-consistent. We did not average the two runs in this case because there is a substantial mismatch between the two at $z < -25$ since the abundance of these most luminous galaxies, at the exponential tail, depends more strongly on large-scale environmental density. We see that from $z = 0$ (red circles) to $z = 1.6$ (black triangles) there is a trend that light density increases with increasing redshift, in accord with the same trend for SFR density seen in Figure 1. It is also seen that the relative contribution to the light density of galaxies at the most luminous end as well as the luminosity of the most luminous galaxies increases with increasing redshift from $z = 0$ to $z = 1.6$. This particular manifestation is in excellent agreement with the apparent downsizing phenomenon first pointed out by Cowie et al. (1996; see Figures 6, 20, 24 therein). As we will show later, the underlying reason for this apparent downsizing phenomenon is simply that the luminosity function in rest-frame z (or in rest-frame K band, as shown in Cowie et al. 1996) becomes brighter with increasing redshift from $z = 0$ to $z \sim 1.6$. While the brightening with increasing redshift is across the entire spectrum of galaxy masses, it is differential where sSFR as a function of stellar mass has a negative slope that steepens with decreasing redshift, as shown in Figure 6 next.

Figure 6 shows the distribution of galaxies in the sSFR– M_{star} plane at $z = (0, 0.5, 1.6, 3.1)$, where each galaxy is also encoded with the average gas entropy at its virial radius—a higher entropy corresponds to a larger circle. The physical importance of gas entropy will become apparent later. The horizontal line

in each panel indicates the value of sSFR at which the galaxy would double its stellar mass in one concurrent Hubble time. We see that at $z = 3.1$ (bottom right panel) most galaxies lie above the horizontal line and sSFR is nearly independent of stellar mass, indicating that all galaxies at this redshift are growing at a similar and rapid pace. As we will show later (see Figure 12), the cold gas inflow rate significantly exceeds SFR, indicating that SF is demand based and self-regulated. Comparison of the four panels clearly shows that a progressively larger fraction of galaxies of all masses downcross the horizontal line with decreasing redshift, with larger galaxies starting that migration earlier and generally at a faster pace than less massive galaxies. It is quite visible that the downcrossing of galaxies over the horizontal line is accompanied by orders of magnitude increases in gas entropy at the virial radii of these galaxies, i.e., circles get much larger moving downward. It is seen that some galaxies of all masses from C run occupy the lower quarter of the lower redshift (upper left and upper right) panels that have the lowest sSFR and largest entropies (large circles); these are galaxies in high entropy cluster environments. The negative slope of the sSFR as a function of stellar mass appears to steepen with decreasing redshift, which will be quantified in Figure 7. As a result, by $z = 0$, only a significant fraction of galaxies of stellar mass less than $\sim 10^{10} M_{\odot}$ can still double their mass in a Hubble time and they are mostly in the V run (i.e., not in overdense regions), while the vast majority of larger galaxies have lost that ability. A comparison of red (galaxies from C run) and blue circles (galaxies from V run) as well as substantial dispersions of sSFR at a fixed stellar mass within each run indicates that

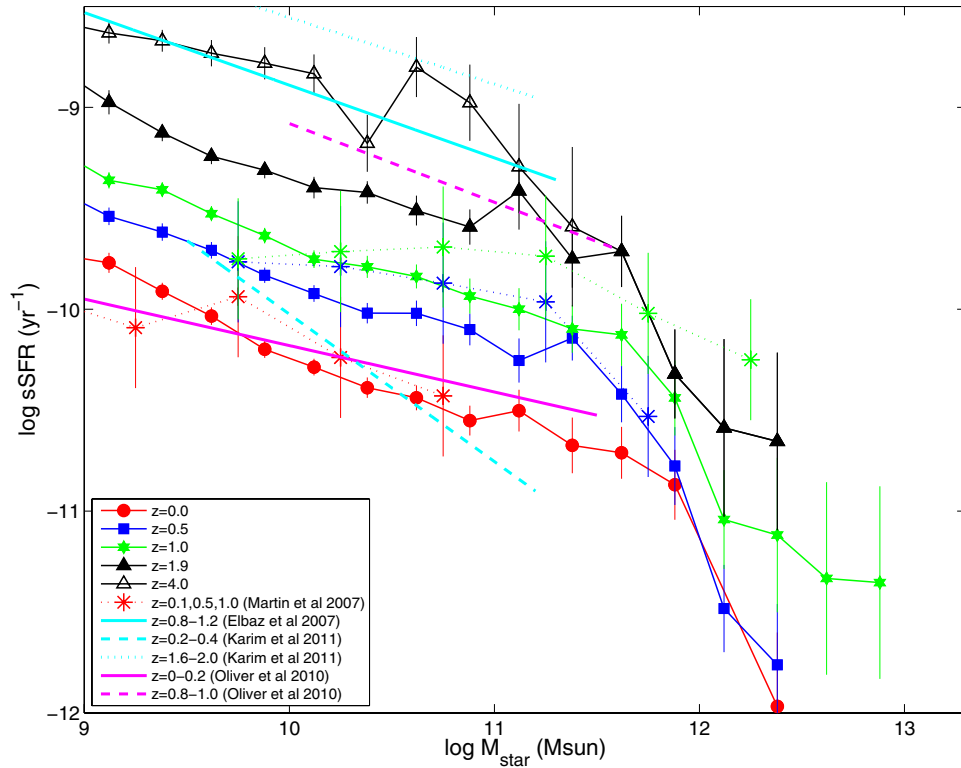


Figure 7. Average sSFR as a function of stellar mass at redshifts $z = (0, 0.5, 1.6, 1.9, 4.0)$ for both C (solid symbols) and V runs (open symbols) with 1σ Poisson error bars. The IR-to-UV observational data points are from Martin et al. (2007) (red, blue, and green asterisks for $z = 0.1$, $z = 0.5$, and $z = 1$, respectively) and are shown exactly as observed; a fit to the FIR observations of Elbaz et al. (2007) at $z = 0.8-1.2$ is shown as the solid cyan line; radio observations of Oliver et al. (2010) are shown as the solid and dashed magenta lines, respectively, for $z = 0-0.2$ and $z = 0.8-1$; radio observations of Karim et al. (2011) are shown as the dashed and dotted cyan lines for $z = 0.2-0.4$ and $z = 1.6-2$, respectively. All results are based on or converted to the standard Salpeter IMF.

(A color version of this figure is available in the online journal.)

there are substantial variations among galaxies of the same mass starting at $z = 1.6$ that must depend on variables other than just the contemporary galaxy mass. As will be shown and discussed extensively subsequently, environmental dependence plays the most fundamental role in shaping the formation and evolution of galaxies, and we find that the gas entropy at the virial radius of each galaxy is a useful variable for understanding the underlying physical cause.

Figure 7 shows the mean sSFR as a function of stellar mass at redshifts $z = (0, 0.5, 1.6, 1.9, 4.0)$. We see that simulations show a trend of steepening slope with decreasing redshift, visually noticed in Figure 6 above, which is generally consistent with observations. The agreement of sSFR between our simulations and observations of Martin et al. (2007; red asterisks), Oliver et al. (2010; solid magenta line), and Karim et al. (2011; dashed cyan line) is reasonably good, within the range of uncertainties of observations; while the UV-selected galaxies from observations of Martin et al. (2007; red asterisks) may be expected to show a flatter slope compared to mass-selected radio galaxies, no such trend is seen, perhaps indicative of large uncertainties in either or both types of observations. Currently, the uncertainties in the observed data at higher redshifts are also larger, as evidenced by the differences in amplitude among the shown observations of Elbaz et al. (2007), Oliver et al. (2010), and Karim et al. (2011) and others (not shown here). Nonetheless, there is unequivocal evidence of a negative slope of sSFR as a function of stellar mass in observations of all redshifts, in broad agreement with simulations. The evolution of the slope with redshift is less clean cut in both simulations and observations, where

the former indicates that power laws do not provide good fits and simulated results become noisy toward high redshift (due to a smaller galaxy sample), whereas the latter are seen to have substantial uncertainties.

In Figure 8 we plot the maximum and mean SFR as a function of stellar mass for seven different redshifts $z = (0, 0.5, 1.0, 1.6, 2.5, 3.1, 4.0)$ for both C (left panel) and V (right panel) runs. One striking result that is best seen in this plot is that the maximum SFR of galaxies at a given mass increases with increasing redshift up to $z_{\max} = 1.6-3.1$. Beyond z_{\max} , that uptrend for maximum SFR at a fixed mass stops and appears to become static. Interestingly, the mean SFR at a fixed mass continues to increase up to the highest redshift shown and the ratio of maximum SFR to mean SFR at a fixed mass continues to shrink, reaching a value of 1–3 in the range $z = 2-4$, suggesting that at high redshift galaxy formation becomes more “uniform.” The second striking result is that the curves are nearly parallel to one another in the C run, suggesting that SFR of galaxies of different masses evolve with redshift at similar rates. This point was noted earlier observationally, first by Zheng et al. (2007; see their Figures 1, 2). As shown in Figure 7, the rate of change of sSFR for galaxies of different mass galaxies is, however, not exactly constant across the mass spectrum. We see very clearly here by comparing the two panels in Figure 8 that this differential at low redshift can be attributed, to a large degree, to less massive galaxies in the V run, i.e., in a low density environment, that refuse to join the dimming trend of galaxies in a high density environment. The physical reason for this will be made clear in Section 3.2.

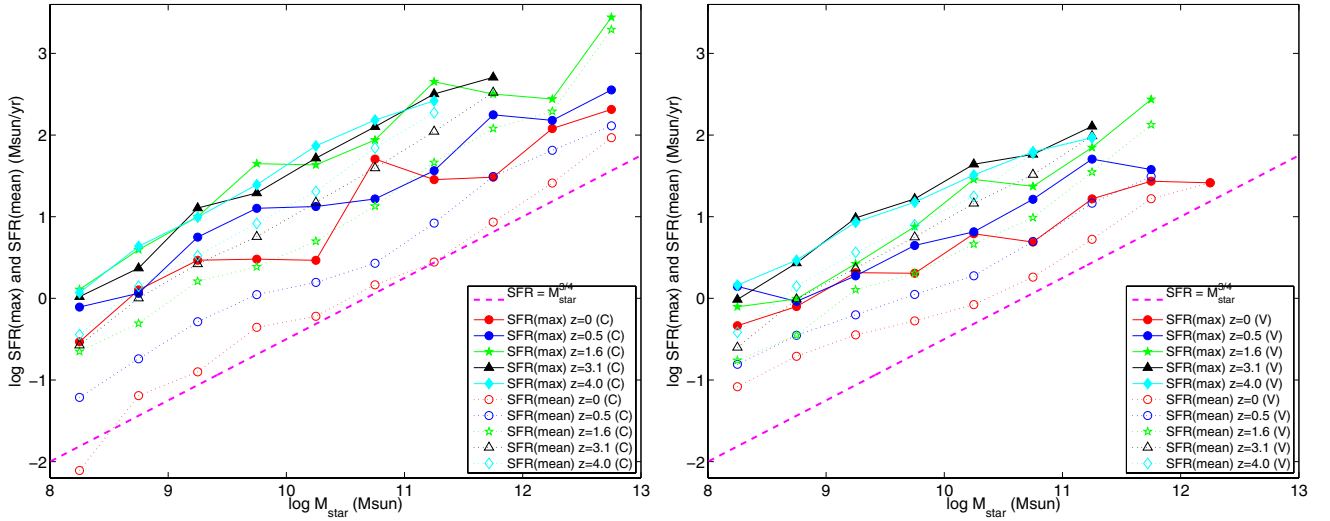


Figure 8. Maximum (solid symbols) and mean SFR (open symbols) as a function of stellar mass at redshifts $z = (0, 0.5, 1.0, 1.6, 2.5, 3.1)$ for both C (left) and V (right) runs. The dashed magenta line has a slope of $3/4$; it is not a fit to the curves but to guide the eye to see the general trend.

(A color version of this figure is available in the online journal.)

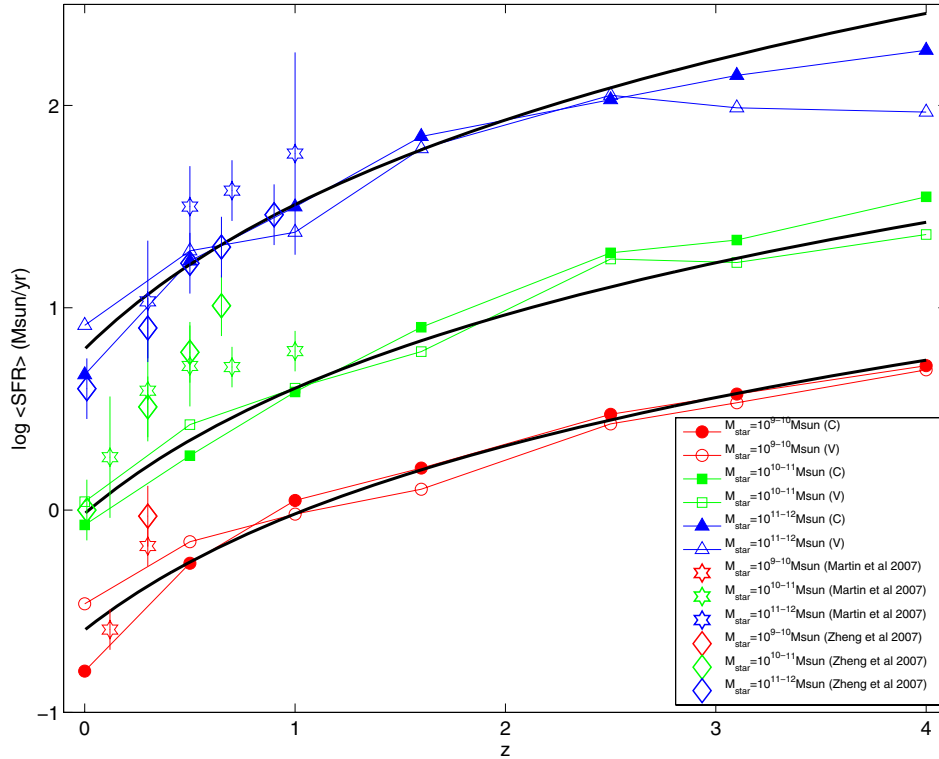


Figure 9. Mean SFR for galaxies of stellar mass in three bins, 10^9 – 10^{10} (red circles), 10^{10} – 10^{11} (green squares), and 10^{11} – $10^{12} M_{\odot}$ (blue triangles), as a function of redshift. The solid symbols are from C run and open symbols from V run. The overplotted black curves are first-order polynomial fits to the three mass bins, averaged over C and V run curves. Also shown as hexagons and diamonds are observations from Martin et al. (2007) and Zheng et al. (2007), respectively.

(A color version of this figure is available in the online journal.)

We note that beyond z_{\max} the mass at the high end is truncated at progressively smaller values with increasing redshift. This sharp cutoff at the high end may be somewhat artificial due to the limited simulation box size we have, but largely reflects the hierarchical nature of growth of dark matter halos in the standard cold dark matter model. As we have shown earlier in Figures 1 and 5 the SFR density and light density peak at $z \sim 1.5$ – 2 ; this suggests, in combination with what is seen in Figure 8, that the growth of halos with time dominates over the downsizing

trend of SFR down to $z = 1.5$ – 2 from high redshift. Thereafter, astrophysical processes that act upon galaxies at $z < 1.5$ – 2 cause galaxy formation and evolution to deviate from the track of continued hierarchical buildup of dark matter halos, resulting in a trend where the total luminosity density and SFR density decreases with time and differential evolution of galaxies with different masses.

Finally, in Figure 9, we show the redshift evolution of SFR for galaxies in three stellar mass bins: 10^9 – 10^{10} (red circles),

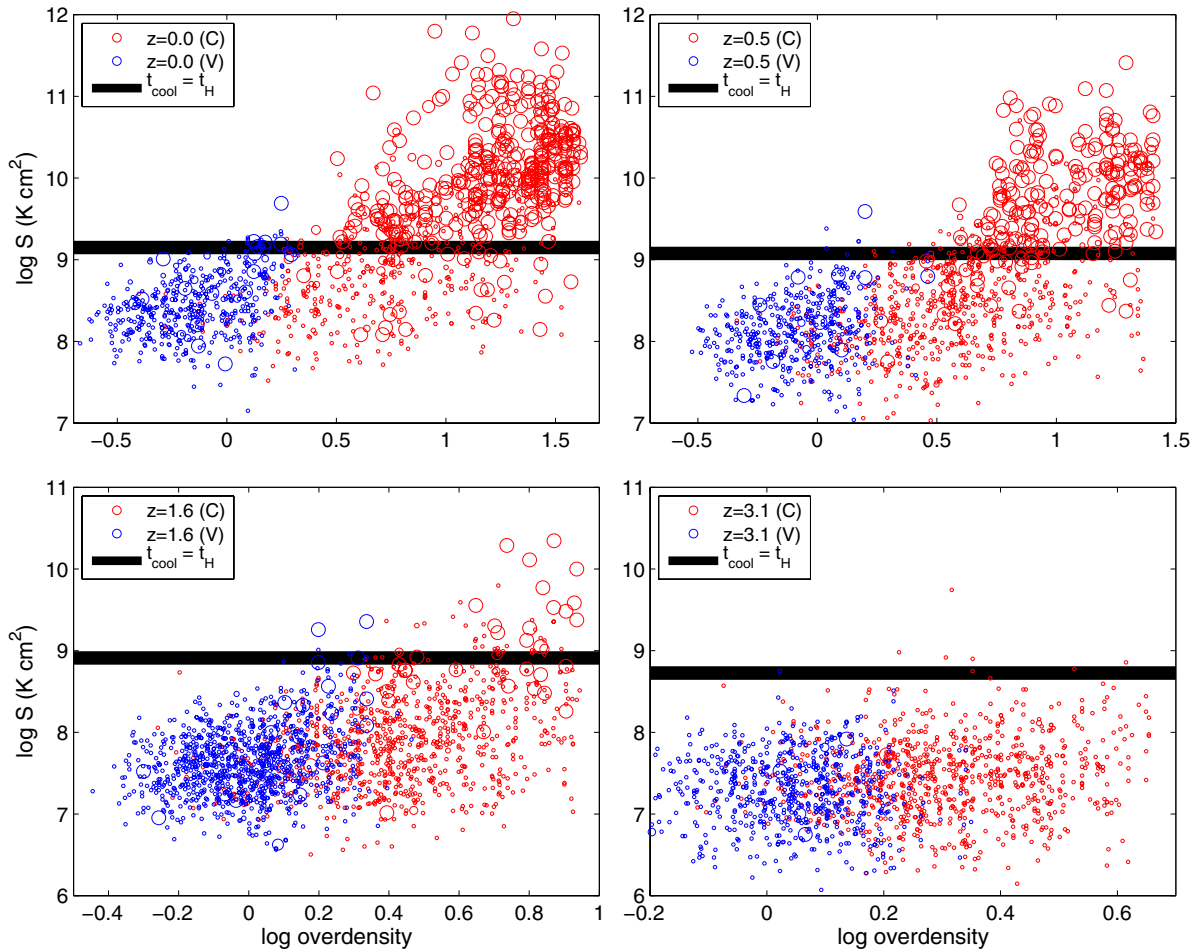


Figure 10. Local mean gas entropy at virial radius as a function of local overdensity smoothed by a Gaussian window of radius $2h^{-1}$ Mpc comoving at redshifts $z = 0$ (top left), $z = 0.5$ (top right), $z = 1.6$ (bottom left), and $z = 3.1$ (bottom right). Each circle is a galaxy from C (red) and V (blue) runs with its size linearly proportional to the inverse of the logarithm of its sSFR; smaller circles correspond to higher sSFR in this representation. Also shown as the horizontal bar is the critical entropy S_{crit} where cooling time is equal to the Hubble time.

(A color version of this figure is available in the online journal.)

Table 1
SFR Evolution as a Function of Stellar Mass

Stellar Mass	$10^9\text{--}10^{10} M_{\odot}$	$10^{10}\text{--}10^{11} M_{\odot}$	$10^{11}\text{--}10^{12} M_{\odot}$
a	−0.59	−0.018	0.80
b	1.9	2.1	2.4

Note. Fitted in the form $\log \text{SFR}/(M_{\odot} \text{ yr}^{-1}) = a(1+z)^b$ —Row 1: Stellar Mass Range; Row 2: a ; Row 3: b .

$10^{10}\text{--}10^{11}$ (green squares), and $10^{11}\text{--}10^{12} M_{\odot}$ (blue triangles). The observational data are still relatively uncertain at higher redshift bins for the low-mass galaxies, as indicated by the difference between different observational determinations. The agreement between simulations and observations are reasonable, especially for the highest mass bin. To best gauge the evolution at low redshift, we decide to fit the simulated results using first-order polynomial fits using only the points at $z < 2$, although higher (e.g., second) order polynomial fits significantly improve the goodness of the fits at $z \geq 2$. The best-fit parameters are tabulated in Table 1. It is evident from the fitting parameters that higher-mass galaxies suffer a steeper drop in SFR in the range $z = 0\text{--}2$ than lower-mass galaxies. This illustrates clearly the differential evolution of sSFR or SFR with redshift for galaxies of different masses.

3.3. Physical Origin: Gravitational Heating of External Gas

We now perform a detailed analysis of the physical conditions of galaxies to understand the cause of the trend of cosmic dimming and its differential nature found in Section 3.2. A useful starting point may be to quantify the evolution of the amount of gas that can cool to feed galaxies. The amount of gas that can cool depends on density, temperature, and metallicity as well as what happens to the gas subsequently, such as shocks, compression, etc. It is therefore highly desirable to project the multidimensional parameter space to as low a dimension space as possible. Gas entropy provides an excellent variable to characterize gas cooling properties. As first insightfully noted by Scannapieco & Oh (2004), the cooling time of any parcel of gas has a minimum value that only depends on the entropy of the gas. Following them we write the gas cooling time in the following form:

$$t_{\text{cool}} = \frac{(3/2)nk_B T}{n_e^2 \Lambda(T)} = S^{3/2} \left[\frac{3}{2} \left(\frac{\mu_e}{\mu} \right)^2 \frac{k_B}{T^{1/2} \Lambda(T)} \right], \quad (1)$$

where n and n_e are total and electron density, respectively; k_B is the Boltzmann's constant, T is temperature, and Λ is cooling function; $\mu = 0.62$ and $\mu_e = 1.18$ for ionized gas that we are

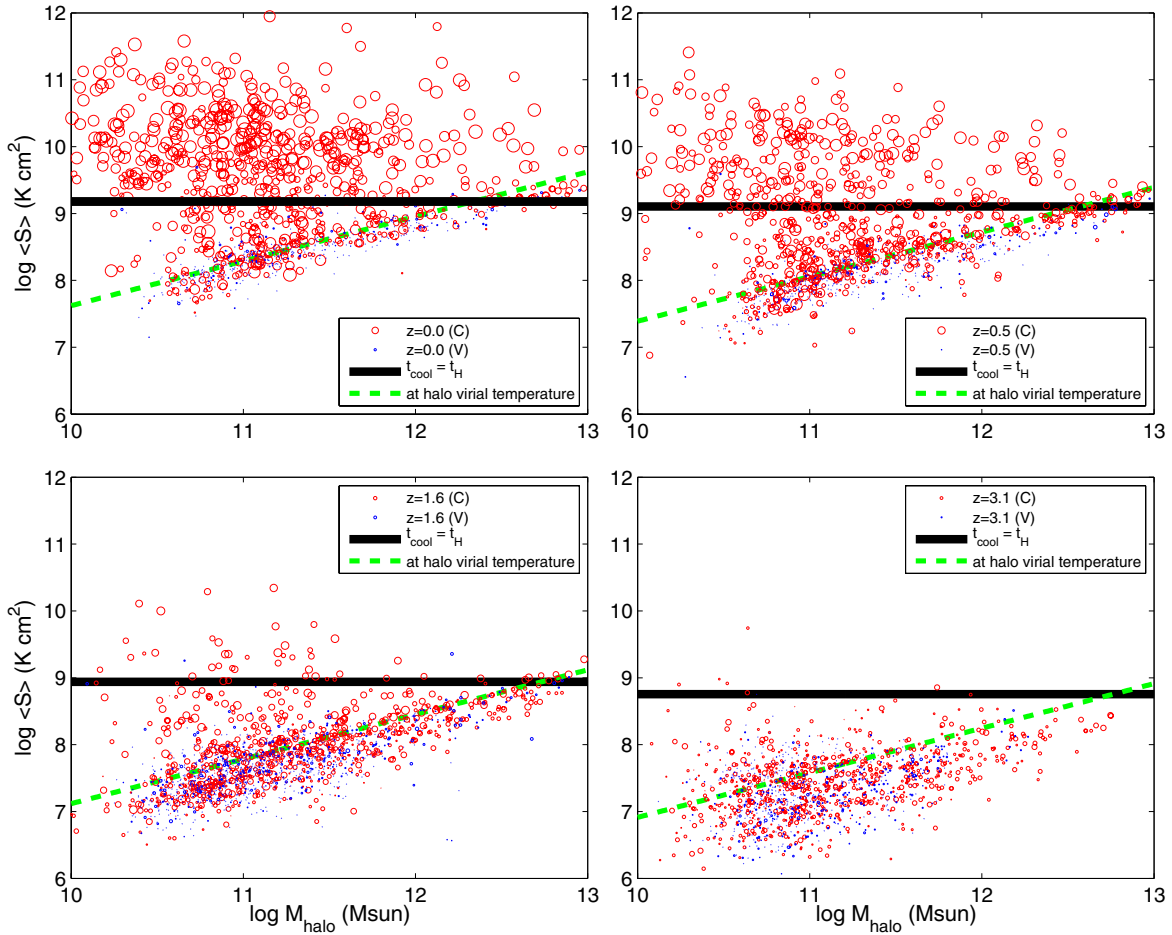


Figure 11. Local mean gas entropy at virial radius as a function of halo mass at redshifts $z = 0$ (top left), $z = 0.5$ (top right), $z = 1.6$ (bottom left), and $z = 3.1$ (bottom right). Each circle is a galaxy from C (red) and V (blue) runs with its size proportional to the logarithm of the local overdensity smoothed by a Gaussian window of radius $0.5 h^{-1}$ Mpc comoving. Also shown as the horizontal bar is the critical entropy S_{crit} where cooling time is equal to the Hubble time. The inclined line indicates the gas entropy at virial radius if the temperature is exactly equal to the virial temperature of the halo.

(A color version of this figure is available in the online journal.)

concerned with; and S is the gas entropy defined as

$$S \equiv \frac{T}{n^{2/3}} \quad (2)$$

in units of K cm^2 . At a fixed S the cooling time is inversely proportional to $T^{1/2}\Lambda(T)$. The cooling function $\Lambda(T)$ depends on the gas metallicity, which is found in our simulations to be almost universal at a value of $\sim 0.1 Z_{\odot}$ for gas at virial radii at the redshifts we are interested in here. Adopting a metallicity of $0.1 Z_{\odot}$ the term $T^{1/2}\Lambda(T)$ has a minimum at $T_{\text{min}} \sim 2.3 \times 10^5$ K (we note that reasonable variations in metallicity, say, to $0.3 Z_{\odot}$ from $0.1 Z_{\odot}$, do not materially impact our arguments). Therefore, if $t_{\text{cool}}(T_{\text{min}}) > t_{\text{H}}$, the gas can never cool in a Hubble time because (1) entropy is a non-decreasing quantity in the absence of cooling and (2) cooling will be insignificant within t_{H} given the initial requirement. Subsequent adiabatic compression or expansion does not alter its fate. Any additional input of entropy, e.g., by shocks, would increase the entropy and make it more difficult to cool. Thus, there is a critical value of entropy S_{crit} for any gas above which gas can no longer cool. The following fitting formula provides a fit to computed critical entropy S_{crit} for gas metallicity of $0.1 Z_{\odot}$ with an accuracy of a few percent over the entire redshift range $z = 0-7$:

$$\log[S_{\text{crit}}/(\text{K cm}^2)] = 9.183 - 0.167z + 0.0092z^2. \quad (3)$$

In Figure 10 we place each galaxy in the entropy-overdensity parameter plane at four redshifts ($z = 0, 0.5, 1.6, 3.1$). The overdensity is defined to be the dark matter density, smoothed by a Gaussian function of radius $2 h^{-1}$ Mpc comoving, divided by the global mean dark matter density. We see that at $z = 3.1$ the entropy of almost all galaxies is located below the critical entropy line, indicating that no significant amount of gas at the virial radius has been heated. One should note that once a gas element has upcrossed the critical entropy S_{crit} , it will not fall back below it again. Therefore, for most galaxies, the moment that it upcrosses S_{crit} marks the beginning of the cold gas starvation phase because galaxies tend to move to higher density, higher entropy regions with time. The size of each circle in Figure 10 is linearly proportional to the inverse of the logarithm of the sSFR of each galaxy. We see that galaxies above the S_{crit} line have dramatically larger circles, i.e., have lower sSFR. It is also interesting to see that galaxies that upcross the S_{crit} line do so only in overdense region (smoothed by a Gaussian radius of $2 h^{-1}$ Mpc). This is clear and powerful evidence that the differential dimming of galaxies is caused by heating of gas in overdense regions; in other words, galaxy formation and long-term evolution are determined by external supply of cold gas, which in turn depends on overdensity on intermediate scales (~ 1 Mpc) that dictate the entropy of shock-heated gas.

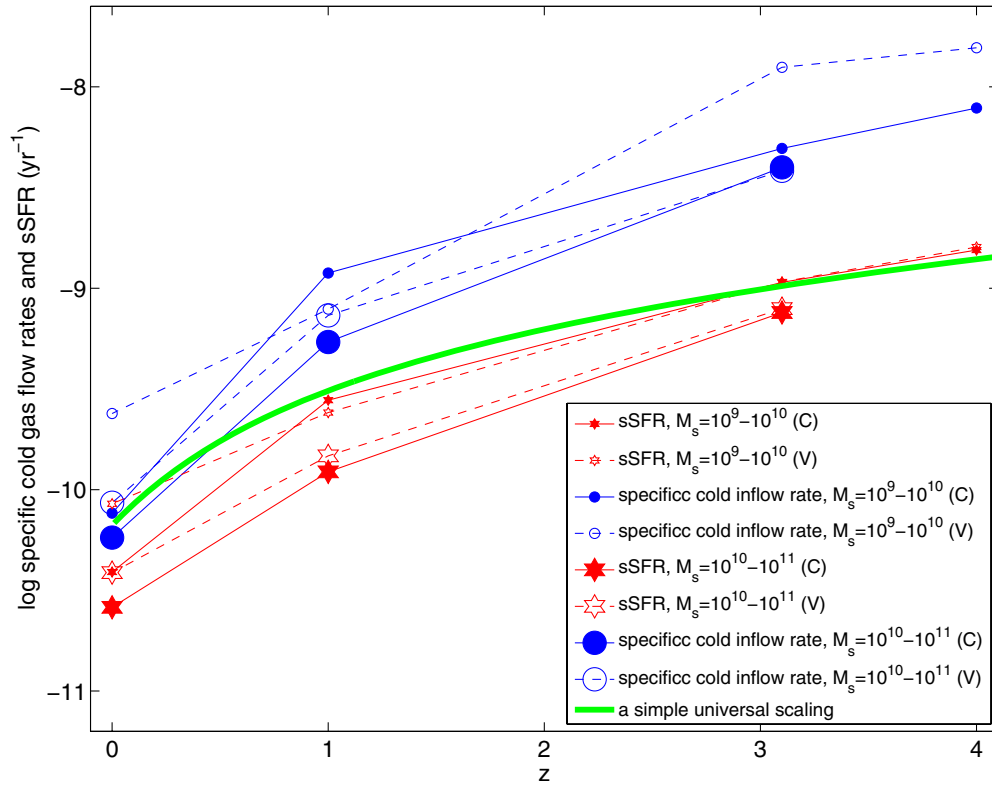


Figure 12. Mean specific cold gas inflow rate (defined to be the cold gas inflow rate per unit stellar mass) and mean sSFR for galaxies in two different stellar mass bins for C and V runs. The cold gas is defined to be that with cooling time less than the dynamic time of the galaxy. Also shown as the solid green curve is the general scaling of gas inflow rate, which is assumed to be proportional to $4\pi r_v^2(z)v_v(z)\rho^3(z)$, where r_v , v_v , and $\rho(z)$ are redshift-dependent virial radius, virial velocity, and mean gas density, respectively.

(A color version of this figure is available in the online journal.)

To help further understand this, in Figure 11, we plot the galaxies in the entropy-halo mass parameter plane at four redshifts. Also shown as the dashed green line in each panel is the gas entropy at virial radius, if the temperature is heated up to the virial temperature of the host halo itself. One notices that at $z = 3.1$ when no galaxies more massive than $\sim 5 \times 10^{12} M_\odot$ have formed, virial heating due to formation of halos is insufficient to upcross the entropy barrier. This is the redshift range where an ample amount of cold gas is available to feed galaxy formation, resulting in sSFR that is very weakly mass dependent and galaxy formation in the “upsizing” domain, in concert with the hierarchical buildup of dark matter halos.

At lower redshifts, the formation of larger halos more massive than $\sim 1 \times 10^{13} M_\odot$ (i.e., groups and clusters) as well as the collapse of larger waves due to the formation of large-scale structures (filaments and walls) raises a progressively larger fraction of regions to higher entropy than S_{crit} . This causes a dichotomy in the entropy distribution, especially at the low halo mass end ($\leq 10^{11} M_\odot$) as follows. There is a branch of low-mass galaxies in low density environments, as evidenced by their small circle sizes, which are located along or below the green line in Figure 11 and have entropies comparable to or lower than what is produced due to adiabatic shock heating accompanying the formation of the halos themselves. These small galaxies correspond to galaxies in the upper left corner in Figure 6 that are still able to double their mass in a Hubble time. Then there is another branch of small galaxies that lie above the S_{crit} line and are in overdense regions, as evidenced by their large circle sizes. These small galaxies are red and dead, corresponding to dwarf galaxies in heated filaments and group/cluster environments.

Generally, the gas entropy of galaxies above the green dashed line is higher than what virial shock heating due to the formation of the halo itself produces; therefore, all these galaxies above the green line are in essence “satellite” galaxies within a large halo (such as a group or cluster) or, if one were to generalize it, “satellite” galaxies in a gravitational shock-heated region due to collapse of large-scale structure (filaments or pancakes), not necessarily virialized. The concentration of galaxies with entropy along the green line is due to virial shock heating of halo itself, i.e., the primary galaxy. It is striking that even at $z = 0$ there is only a very handful of (blue circle) galaxies with mass greater than $10^{12} M_\odot$ that lie above the S_{crit} from the V run. Taken together, this is unequivocal evidence that it is the external gas heating that drives the gas supply and hence SF and galaxy evolution; the absence of such heating in the V run has allowed galaxies there to remain active in SF at present.

Figure 12 shows the mean specific cold gas inflow rate (defined to be the cold gas inflow rate per unit stellar mass and cold gas is defined to be gas that has a cooling time less than the galaxy dynamical time at the virial radius) and mean sSFR for galaxies in two different stellar mass bins for C and V runs. Several points are worth noting. First, we see that the cold gas inflow rates are generally higher than SFRs, suggesting self-regulation of SF, mostly due to feedback from SF. Second, the ratio of cold gas inflow rate to SFR decreases with decreasing redshift, pointing to a gradual transition of SF regimes from gas demand based at high redshift to gas supply based at low redshift. Third, the rough similarity between the evolution of the gas inflow rate based on a simple scaling and

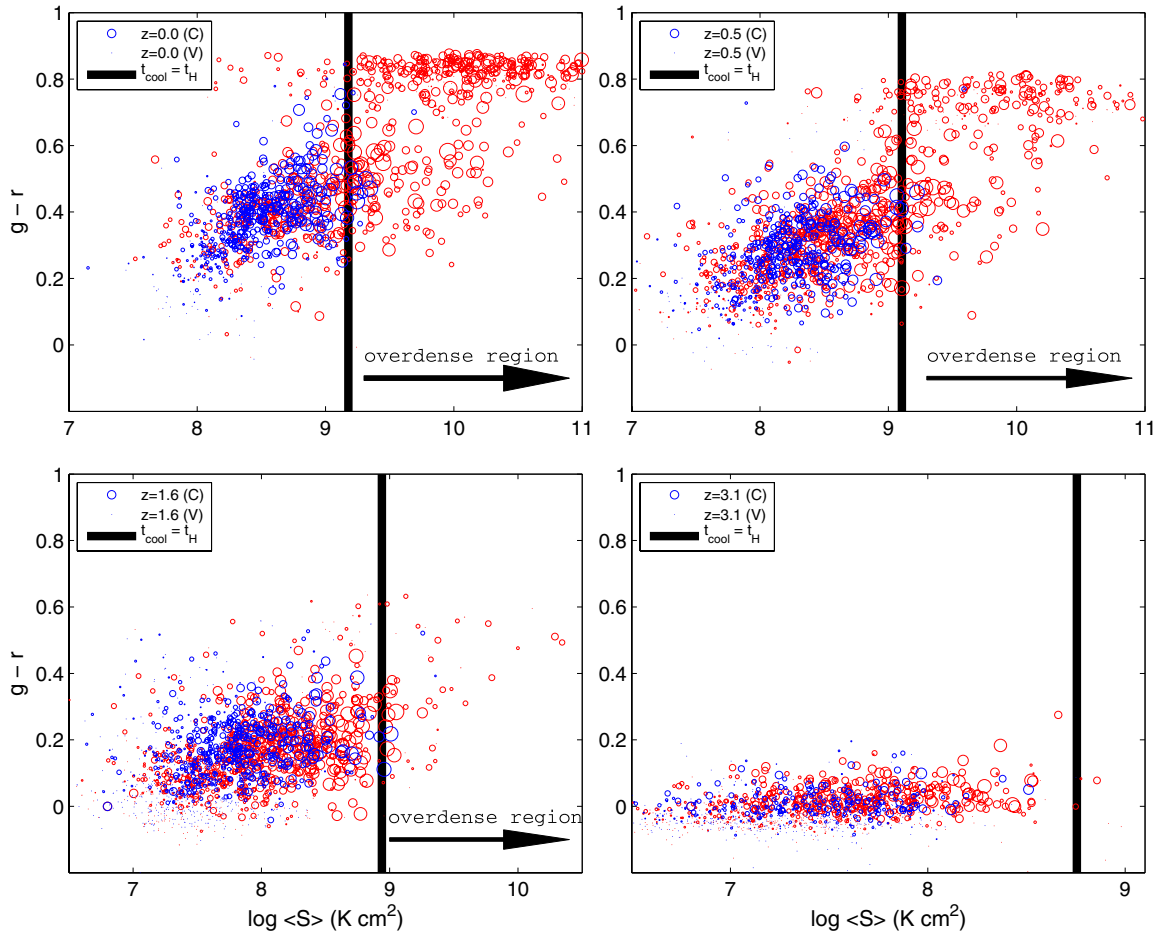


Figure 13. SDSS $g-r$ color of galaxies as a function of local mean gas entropy at the virial radius at $z = 0$ (top left), $z = 0.5$ (top right), $z = 1.6$ (bottom left), and $z = 3.1$ (bottom right). The galaxies in C run are shown in red and those in V run in blue. The size of each circle is proportional to the logarithm of the galaxy stellar mass. Also shown as the vertical line is the critical entropy S_{crit} where cooling time is equal to the Hubble time.

(A color version of this figure is available in the online journal.)

the actual computed rates suggests that the bulk of the cosmic dimming trend with decreasing redshift can be attributed to the decrease of mean density of the universe with increasing time and the evolution of the Hubble constant (or density parameter). Finally, the gravitational heating effects add a differentiating process on the top of this general dimming trend, evident here by the different steepening with decreasing redshift of the specific gas inflow rates and SFR at lower redshifts among galaxies of different masses and galaxies in different environments (C versus V runs).

Finally, in Figure 13, we place galaxies in the color–entropy plane. Four things are immediately noticeable. First, the vast majority of galaxies are blue (in color, not the color of the plotted circles) and there is no strong evidence of bimodality in color at $z \geq 1.6$. The red peak at these high redshifts is somewhat suppressed artificially, due to limited sizes of the simulation boxes that do not contain large halos at these redshifts. Second, at $z = 0-0.5$, almost all galaxies in the V run occupy the blue peak at $g-r \sim 0.2-0.6$ with very few in the red peak. Third, the vast majority of galaxies on the left side of the critical entropy line are in the blue cloud, as they should be. Fourth, there is a significant number of galaxies on the right side of the critical entropy line that appear blue and have masses covering a comparable range compared to those in the red sequence. Thus, Figure 13 gives a physical underpinning for the well-known color–magnitude diagram of galaxies (e.g., Baldry et al. 2004).

The existence of the cold-gas-starved yet blue galaxies indicates that external gas heating is the driving force causing these blue galaxies to migrate upward in Figure 13 to ultimately join the red sequence. The fact that many galaxies in the V run, though having higher sSFR than those in the C run (see Figures 6, 9, 10, and 12), both remain blue (as they should, given the high sSFR) and have low entropies suggests that SF is not the primary driver for the color migration. An internal driver, such as feedback from starbursts or AGNs, may play a role in quenching SF in a small fraction of galaxies that experience immense starbursts (e.g., caused by major mergers); but the situation is unclear at present.

3.4. Predictions

Several manifestations of downsizing trends should by now be understood, including: (1) the epoch of major stellar mass buildup in massive galaxies is substantially earlier than the epoch of mass buildup in low-mass galaxies, (2) the SF and stellar mass buildup are accelerated in overdense regions compared to less overdense regions, (3) massive galaxies are on average older than less massive galaxies, (4) galaxies of all masses, on average, get bluer with increasing redshift, (5) galaxy self-metal enrichment shifts from high-mass galaxies at high redshift to lower-mass galaxies at lower redshift, all in broad agreement with a variety of observations (e.g., Kodama et al. 2004; Pérez-González et al. 2005; Bundy et al. 2006; Noeske et al. 2007;

Zheng et al. 2007; Martin et al. 2007; Tresse et al. 2007; Buat et al. 2007; Lehmer et al. 2008; Mobasher et al. 2009; Hartley et al. 2010; Cirasuolo et al. 2010; Karim et al. 2011; Pilyugin & Thuan 2011). This model provides a coherent and unified physical interpretation.

Many other general trends in galaxy formation and evolution that this model would predict have already been confirmed by observations, including: (1) the galaxy color–environment relation (e.g., Blanton et al. 2005), (2) galaxy SF as a function of environment, specifically the dramatic transition at a few cluster virial radii that mark the location of virial shocks (e.g., Gómez et al. 2003), (3) the trend of galaxies having higher sSFR and becoming bluer toward voids from cluster environments (e.g., Kauffmann et al. 2004; Rojas et al. 2004, 2005), and (4) redder galaxies have stronger correlation functions than blue galaxies, irrespective of their luminosities (e.g., Zehavi et al. 2005).

More quantitative analyses and comparisons to observations will be performed elsewhere.

4. CONCLUSIONS

With high resolution and a physically sound treatment of relevant physical processes, our state-of-the-art, AMR Eulerian cosmological hydrodynamic simulations reproduce reasonably well some key observables of galaxies as a whole, including luminosity function, color distribution, and SF history. This allows us to examine, in addition, with confidence, some global trends of formation and evolution of galaxies. Several findings are interesting and new.

(1) The overall dimming trend of galaxies of all masses is largely attributable to the evolution of mean cosmic gas density and density parameter. (2) Gravitational shock heating due to the formation of halos and large-scale structure adds a differential layer on top of this general global dimming trend. (3) As a result, the mean sSFR is a monotonically increasing function of redshift at a given galaxy mass. (4) The mean sSFR is a monotonically decreasing function of galaxy mass at a given redshift and steepens with decreasing redshift, which overwhelmed the continued hierarchical growth of halos at low redshift range $z = 0$ –2 and is the underlying physical driver for some apparent “anti-hierarchical” manifestations of some galaxy properties. (5) The SFR function is a convolution of sSFR and galaxy mass function—it increases from $z = 0$ to $z \sim 2$ and thereafter decreases toward (i.e., an upsizing trend) higher redshift. (6) Although the buildup of dark matter mass and stellar mass are not necessarily exactly parallel to one another, the overall trend for both is still hierarchical.

The underlying physical cause for Trend (2) above is as follows. With time, more regions are heated to higher temperatures due to the formation of large halos (such as groups and clusters) and large-scale structures that result in a progressively larger fraction of halos inhabiting regions where gas has too high an entropy to cool to continue feeding the residing galaxies. Thus, overdense regions enter the cold gas starvation phase earlier than lower density regions. Because larger halos tend to reside in more overdense regions than smaller halos, the net differential effects are that larger galaxies fall below the general dimming trend at higher redshift than less massive galaxies, the sSFR as a function of galaxy mass steepens with time, and galaxies with high sSFR gradually shift to lower density environments. By $z = 0$, galaxies with high sSFR (such that they may be categorized as blue) have almost entirely left the cluster environments and can be found in fields and voids. Thus, the processes that drive galaxy evolution are mostly external at $z \lesssim 2$, due to gravi-

tational heating of either its own halo formation, or formation of the primary galaxy or group/cluster halo in the case of a satellite galaxy, or collapse of embedding large-scale structures such as filaments or Zeldovich pancakes, which at low redshift correspond to the cosmic web of warm–hot intergalactic medium (e.g., Cen & Ostriker 1999).

We also find that the cold gas starvation due to gravitational heating provides a viable physical mechanism to explain the observed migration of galaxies to the red sequence from the blue cloud as well as many other phenomena, such as the observed color–density relation, the trend of galaxies becoming bluer in lower density environment, and others. Several predictions are made in Section 3.4.

These findings also imply that the concept of two modes of gas accretion onto galaxies (e.g., Kereš et al. 2005; Dekel & Birnboim 2006), while very useful to crystallize some aspects of galaxy formation, may need to be mended to be globally applicable because the amount of cold as well as hot gas around a galaxy depends on both its mass and its external environment (and perhaps its own history). For example, a small galaxy in a cluster environment would have a very different mix of cold and hot gas components from a galaxy of the same mass in a void environment, with the latter having a much larger cold gas fraction than the former. We further note that galaxy formation recipes, such as those used in semi-analytic modeling, may need to include the important external effects found here to be physically realistic. In essence, realistic treatments of galaxy formation have to be multivariant, not just dependent on the contemporary halo mass.

I thank Dr. M. K. R. Joung for help with generating initial conditions for the simulations and running a portion of the simulations, and Greg Bryan and John Wise for help with Enzo code. I also thank Dr. D. Christopher Martin for kindly providing plotting data for observations. Computing resources were in part provided by the NASA High-End Computing (HEC) Program through the NASA Advanced Supercomputing (NAS) Division at Ames Research Center. This work is supported in part by grants NNX08AH31G and NAS8-03060. The simulation data are available from the author upon request.

REFERENCES

- Baldry, I. K., Glazebrook, K., Brinkmann, J., et al. 2004, *ApJ*, **600**, 681
- Bauermeister, A., Blitz, L., & Ma, C.-P. 2010, *ApJ*, **717**, 323
- Blanton, M. R., Eisenstein, D., Hogg, D. W., Schlegel, D. J., & Brinkmann, J. 2005, *ApJ*, **629**, 143
- Blanton, M. R., Hogg, D. W., Bahcall, N. A., et al. 2003a, *ApJ*, **594**, 186
- Blanton, M. R., Hogg, D. W., Bahcall, N. A., et al. 2003b, *ApJ*, **592**, 819
- Bouwens, R. J., Illingworth, G. D., Franx, M., & Ford, H. 2007, *ApJ*, **670**, 928
- Bower, R. G., Benson, A. J., Malbon, R., et al. 2006, *MNRAS*, **370**, 645
- Brinchmann, J., Charlot, S., White, S. D. M., et al. 2004, *MNRAS*, **351**, 1151
- Bruzual, G., & Charlot, S. 2003, *MNRAS*, **344**, 1000
- Bryan, G. L. 1999, *Comput. Sci. Eng.*, **1**, 46
- Bryan, G. L., & Norman, M. L. 2000, *IMA*, **117**, 165
- Buat, V., Takeuchi, T. T., Iglesias-Páramo, J., et al. 2007, *ApJS*, **173**, 404
- Bundy, K., Ellis, R. S., Conselice, C. J., et al. 2006, *ApJ*, **651**, 120
- Caputi, K. I., Lagache, G., Yan, L., et al. 2007, *ApJ*, **660**, 97
- Cen, R. 2010, arXiv:1010.5014
- Cen, R., Kang, H., Ostriker, J. P., & Ryu, D. 1995, *ApJ*, **451**, 436
- Cen, R., Nagamine, K., & Ostriker, J. P. 2005, *ApJ*, **635**, 86
- Cen, R., & Ostriker, J. P. 1992, *ApJ*, **399**, L113
- Cen, R., & Ostriker, J. P. 1999, *ApJ*, **514**, 1
- Ceverino, D., Dekel, A., & Bournaud, F. 2010, *MNRAS*, **404**, 2151
- Cirasuolo, M., McLure, R. J., Dunlop, J. S., et al. 2007, *MNRAS*, **380**, 585
- Cirasuolo, M., McLure, R. J., Dunlop, J. S., et al. 2010, *MNRAS*, **401**, 1166
- Cowie, L. L., Songaila, A., Hu, E. M., & Cohen, J. G. 1996, *AJ*, **112**, 839
- Croton, D. J., Springel, V., White, S. D. M., et al. 2006, *MNRAS*, **365**, 11

- Davé, R., Finlator, K., Oppenheimer, B. D., et al. 2010, [MNRAS](#), **404**, 1355
- Dekel, A., & Birnboim, Y. 2006, [MNRAS](#), **368**, 2
- Eisenstein, D., & Hu, P. 1999, [ApJ](#), **511**, 5
- Elbaz, D., Daddi, E., Le Borgne, D., et al. 2007, [A&A](#), **468**, 33
- Franzetti, P., Scodreggio, M., Garilli, B., et al. 2007, [A&A](#), **465**, 711
- Gnedin, N. Y., Tassis, K., & Kravtsov, A. V. 2009, [ApJ](#), **697**, 55
- Gómez, P. L., Nichol, R. C., Miller, C. J., et al. 2003, [ApJ](#), **584**, 210
- Governato, F., Brook, C. B., Brooks, A. M., et al. 2009, [MNRAS](#), **398**, 312
- Haardt, F., & Madau, P. 1996, [ApJ](#), **461**, 20
- Hartley, W. G., Almaini, O., Cirasuolo, M., et al. 2010, [MNRAS](#), **407**, 1212
- Heckman, T. M. 2001, in ASP Conf. Ser. 240, Gas and Galaxy Evolution, ed. J. E. Hibbard, M. Rupen, & J. H. van Gorkom (San Francisco, CA: ASP), 345
- Hopkins, A. M., & Beacom, J. F. 2006, [ApJ](#), **651**, 142
- Hopkins, P. F., Hernquist, L., Cox, T. J., et al. 2006, [ApJS](#), **163**, 1
- Joung, M. R., Cen, R., & Bryan, G. L. 2009, [ApJ](#), **692**, L1
- Karim, A., Schinnerer, E., Martínez-Sansigre, A., et al. 2011, [ApJ](#), **730**, 61
- Kauffmann, G., White, S. D. M., Heckman, T. M., et al. 2004, [MNRAS](#), **353**, 713
- Kennicutt, R. C., Jr. 1998, [ARA&A](#), **36**, 189
- Kereš, D., Katz, N., Weinberg, D. H., & Davé, R. 2005, [MNRAS](#), **363**, 2
- Kodama, T., Yamada, T., Akiyama, M., et al. 2004, [MNRAS](#), **350**, 1005
- Komatsu, E., Smith, K. M., Dunkley, J., et al. 2011, [ApJS](#), **192**, 18
- Lehmer, B. D., Brandt, W. N., Alexander, D. M., et al. 2008, [ApJ](#), **681**, 1163
- Martin, D. C., Small, T., Schiminovich, D., et al. 2007, [ApJS](#), **173**, 415
- Mayer, L., Kazantzidis, S., Madau, P., et al. 2007, [Science](#), **316**, 1874
- McCarthy, I. G., Schaye, J., Bower, R. G., et al. 2011, [MNRAS](#), **412**, 1965
- Mobasher, B., Dahlen, T., Hopkins, A., et al. 2009, [ApJ](#), **690**, 1074
- Noeske, K. G., Weiner, B. J., Faber, S. M., et al. 2007, [ApJ](#), **660**, L43
- Oke, J. B. 1974, [ApJS](#), **27**, 21
- Oliver, S., Frost, M., Farrah, D., et al. 2010, [MNRAS](#), **405**, 2279
- O'Shea, B. W., Bryan, G., Bordner, J., et al. 2004, arXiv:astro-ph/0403044
- Pérez-González, P. G., Rieke, G. H., Egami, E., et al. 2005, [ApJ](#), **630**, 82
- Pilyugin, L. S., & Thuan, T. X. 2011, [ApJ](#), **726**, L23
- Reddy, N. A., & Steidel, C. C. 2009, [ApJ](#), **692**, 778
- Rojas, R. R., Vogeley, M. S., Hoyle, F., & Brinkmann, J. 2004, [ApJ](#), **617**, 50
- Rojas, R. R., Vogeley, M. S., Hoyle, F., & Brinkmann, J. 2005, [ApJ](#), **624**, 571
- Scannapieco, E., & Oh, S. P. 2004, [ApJ](#), **608**, 62
- Seymour, N., Ogle, P., De Breuck, C., et al. 2008, [ApJ](#), **681**, L1
- Tresse, L., Ilbert, O., Zucca, E., et al. 2007, [A&A](#), **472**, 403
- Weiner, B. J., Phillips, A. C., Faber, S. M., et al. 2005, [ApJ](#), **620**, 595
- Yan, H., & Windhorst, R. A. 2004, [ApJ](#), **612**, L93
- Zehavi, I., Zheng, Z., Weinberg, D. H., et al. 2005, [ApJ](#), **630**, 1
- Zheng, X. Z., Bell, E. F., Papovich, C., et al. 2007, [ApJ](#), **661**, L41